metals

MDPI

Article

Effect of Al/Mg Ratio on the Microstructure and Phase Distribution of Zn-Al-Mg Coatings

Ziyue Zhang [1,2], Jie Zhang [2,*], Xingyuan Zhao [2], Xin Liu [2], Xuequn Cheng [1], Sheming Jiang [2] and Qifu Zhang [2]

[1] Corrosion & Protection Center, University of Science & Technology Beijing, Beijing 100083, China
[2] National Engineering Laboratory of Advanced Coating Technology for Metals, Central Iron & Steel Research Institute, Beijing100081, China; lxv20032003@163.com (X.L.); jiangsheming@263.net (S.J.)
* Correspondence: zhangj0212@163.com

Abstract: In contrast with studies such as those on the effect of a single elemental variable on Zn-Al-Mg coatings, Mg/Al is considered a variable parameter for evaluating the microstructure of Zn-Al-Mg coatings in this work, and the combined effect of the two elements is also taken into account. The Mg/Al ratios in the continuous hot-dip plating of low-alumina Zn-Al-Mg coatings were 0.63, 0.75, 1.00, 1.25, and 1.63. respectively, and the microstructures of the different coatings were observed using scanning electron microscopy (SEM). The surface elemental distributions of the coatings were analyzed with energy dispersive spectrometry (EDS) and X-ray diffraction (XRD) analysis to understand the phase distributions of the coatings, which mainly consisted of a zinc monomeric phase, a binary eutectic phase ($Zn/MgZn_2$), and a ternary eutectic phase ($Zn/Al/MgZn_2$). Statistical calculations of the phase distributions in colored SEM images were performed using ImageJ-win64 software, comparative analysis of the solidification simulation results was carried out with thermodynamic simulation software (PANDAT-2023), and evaluation of the corrosion resistance of the platings was performed using macroscopic cyclic immersion corrosion experiments. The results show that with the increase in the Mg/Al ratio, the binary eutectic phase in the coatings gradually increased, the variation trend of the ternary eutectic phase was not obvious, and the corrosion resistance of the coatings gradually improved.

Keywords: Zn-Al-Mg coatings; micromorphology; phase distribution; corrosion resistance

check for updates

Citation: Zhang, Z.; Zhang, J.; Zhao, X.; Liu, X.; Cheng, X.; Jiang, S.; Zhang, Q. Effect of Al/Mg Ratio on the Microstructure and Phase Distribution of Zn-Al-Mg Coatings. *Metals* **2023**, *13*, 1963. https://doi.org/10.3390/met13121963

Academic Editor: Marcello Cabibbo

Received: 30 October 2023
Revised: 24 November 2023
Accepted: 28 November 2023
Published: 1 December 2023

Copyright: © 2023 by the authors. Licensee MDPI, Basel, Switzerland. This article is an open access article distributed under the terms and conditions of the Creative Commons Attribution (CC BY) license (https://creativecommons.org/licenses/by/4.0/).

1. Introduction

The hot-dip galvanizing process can effectively slow down the corrosion rate of steel materials, and it is widely used in industries such as automobiles, household appliances, and construction for its economic benefits and good appearance [1,2]. With the development of the industry, the demand for coating properties has become increasingly strict, from the initial pure zinc coatings to the addition of aluminum and then to the rapidly developing high-corrosion-resistant zinc–aluminum–magnesium coatings in recent decades [3–5].

Zinc–aluminum–magnesium coatings are generally divided into three categories (a low-aluminum series with an Al content of 1.0–2.5 wt.%, a medium-aluminum series with an Al content of 6.0%–11 wt.%, and a high-aluminum series with an Al content of 50%–60 wt.%) [6–8]. The main research object of this study was low-aluminum coatings, which are currently also the most widely applied. The performance of zinc–aluminum–magnesium coating products mainly depends on the phase composition and microstructure, and the typical structures include a Zn-rich phase (a spherical and platy structure), a binary $Zn/MgZn_2$ eutectic phase (a coarse platy structure), and a ternary $Zn/MgZn_2/Al$ eutectic phase (a fine platy structure). Studies have shown that the $MgZn_2$ phase is the main reason for the improved corrosion resistance of a coating [9–12]. During the corrosion process, an electric couple is formed between Zn and $MgZn_2$ due to the potential difference between them. The $MgZn_2$ phase acts as an anode, while the Zn-rich phase acts as a cathode, and it

is protected. After $MgZn_2$ dissolves, it provides Mg^{2+} cations and reacts with OH^- to form $Mg(OH)_2$ precipitates, while Zn^{2+} and $Zn(OH)_2$ eventually form ZnO. The precipitation of $Mg(OH)_2$ lowers the pH value, thereby creating the thermodynamic conditions for the formation of the water-insoluble simonkolleite ($Zn_5Cl_2(OH)_8 \cdot H_2O$) [13–15]. However, partial studies show that due to the relatively poor stress–strain behavior of $MgZn_2$, it is easy to produce cracks during deformation processing, which leads to a decrease in the material performance. Therefore, controlling the $MgZn_2$ phase in the coating is a key factor for the coating properties [16,17].

The main differences in the phase compositions and microstructures of coatings depend on the composition and the dip plating process, in which the most important step is the cooling rate after plating [18]. However, considering that the cooling equipment of the actual production line generally only reaches a speed of 5–10 °C/s, increasing the cooling rate further requires a significant cost to retrofit. Therefore, under certain dip plating process conditions, it is highly meaningful to study the influence of the coating solution composition on the coating structure.

In addition, if the composition of the molten pool only contains Zn and Mg, MgO oxide will be formed on the surface of the molten pool. Since the formation of MgO is known to produce pores and cannot form a continuous layer, it cannot protect the melt from further oxidation [19]. Meanwhile, adding a sufficient amount of Al can form a continuous $MgAl_2O_4$ layer on the surface of the plating solution to protect it [20–24].

Therefore, it is necessary to study the effect of the Mg/Al ratio on the microstructure and phase distribution of the plating [25–30]. Jaenam Kim et al. [31] investigated the effect of the Mg/Al ratio on the structure of MgxZny in a hot-dip zinc-Mg-Al coating layer on interstitial-free steel, but the results of the study indicated that the structure of MgxZny was negligibly influenced by the Mg/Al ratio. However, the effect of the Mg-Al ratio on the whole coating structure was not involved in the study, and the study in this paper can fill the blank in this area. The Mg/Al ratio and composition of the hot dip solution have important guiding significance, so this work mainly focused on the influence of the Mg/Al ratio on the phase composition and microstructure of the coating.

In fact, the design of the complete experiment consisted of two parts: the first part was the effect of the simultaneous increase in the magnesium and aluminum elements on the microscopic morphology of the coating for a constant Mg/Al ratio of 1:1, and the results of this study have already been described in a previous paper [32]. This paper is another part of the validation experiment on the effect of a gradual increase in the Mg/Al ratio on the coating within a certain range of elemental contents. The significance of the whole experiment was to determine the microstructure of the coating with the Mg/Al ratio, rather than the effect of a single element or the cooling rate [33,34]. The Mg/Al ratio is useful as a reference for adjusting the composition of the alloy solution in the molten bath as well as controlling the coating properties in actual production. Due to the differences in the consumption rates of various elements in the hot-dipping process, it is difficult to recognize a single element to satisfy the demand of various supplemental alloy ingots, which makes the Mg/Al ratio an influencing factor for evaluating the microstructure of the coating.

2. Experimental Materials and Methods

2.1. Material Preparation

The Zn-Al-Mg coating specimens were prepared with a self-developed hot-dip simulation machine (GCA-IV) in the laboratory, which can emulate actual hot-dip coating production lines under factory conditions, such as the annealing temperature, immersion time, and post-coating cooling rate, which were flexibly controlled. The steel substrate for the coating was a low-carbon interstitial-free (IF) cold-rolled thin plate and was produced by Shougang Corporation. The main route parameters for the specimen preparation are shown in Figure 1. The protective atmosphere for the steel plate annealing was 90% N_2 + 10% H_2, and a purging process with 70% N_2 + 30% H_2 was adopted in the cooling stage, and the cooling rate was controlled by adjusting the atmosphere flow rate. The coating

thickness was controlled at approximately 20 um by adjusting the N_2 gas knife flow rate. The composition and identification numbers of the samples are shown in Table 1. The samples were cut into 10 mm (length) × 10 mm (width) and 30 mm (length) × 60 mm (width) pieces for the micromorphological observation and cyclic immersion corrosion test, respectively. The samples used in the corrosion experiment were edge-sealed with silica gel.

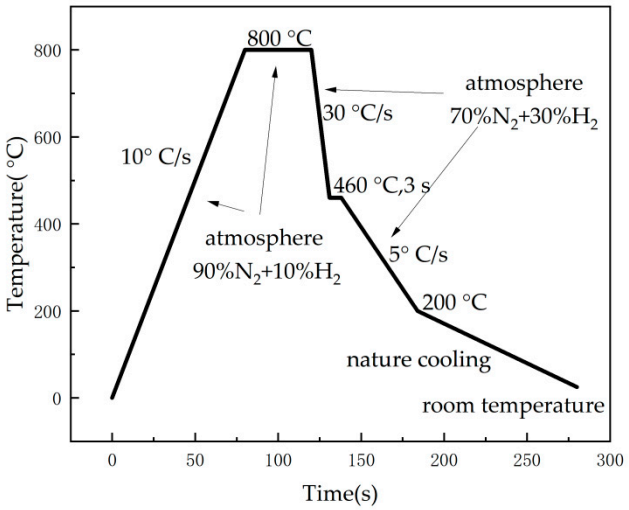


Figure 1. Experimental process control flow chart of hot-dip plating simulator.

Table 1. The compositions of experimental coatings and corresponding Al/Mg ratios.

Sample No.	Component	Mg/Al Ratio	Mg (wt.%) (±0.1)	Al (wt.%) (±0.1)	Zn (wt.%) (±0.1)
ZAM1	Zn-1.6Al-1.0Mg	0.63	1.04	1.62	97.34
ZAM2	Zn-1.6Al-1.2Mg	0.75	1.22	1.62	97.16
ZAM3	Zn-1.6Al-1.6Mg	1.00	1.58	1.61	96.81
ZAM4	Zn-1.6Al-2.0Mg	1.25	2.05	1.59	96.36
ZAM5	Zn-1.6Al-2.6Mg	1.63	2.63	1.58	95.79

2.2. Characterization and Statistics

The microstructures of the ZnAlMg coatings were investigated using an FEI Quant 650-FEG scanning electron microscope (SEM) with energy-dispersive spectroscopy (EDS) analysis for the elemental distributions. The physical phases of the coatings were analyzed with a Bruker D8 ADVANCE X-ray diffractometer with a Co target, a tube current of 40 mA, a tube voltage of 35 kV, and a scanning speed of 2°/min, and a Lynxeye XE detector.

PANDAT-2023 software was used to simulate the solidification phases of the alloy coatings, and the samples were solidified at a cooling rate of 5 °C/S after plating, which was fast and close to non-equilibrium solidification under ideal conditions. Therefore, the Scheil solidification model was suitable due to the coatings' rapid cooling rates.

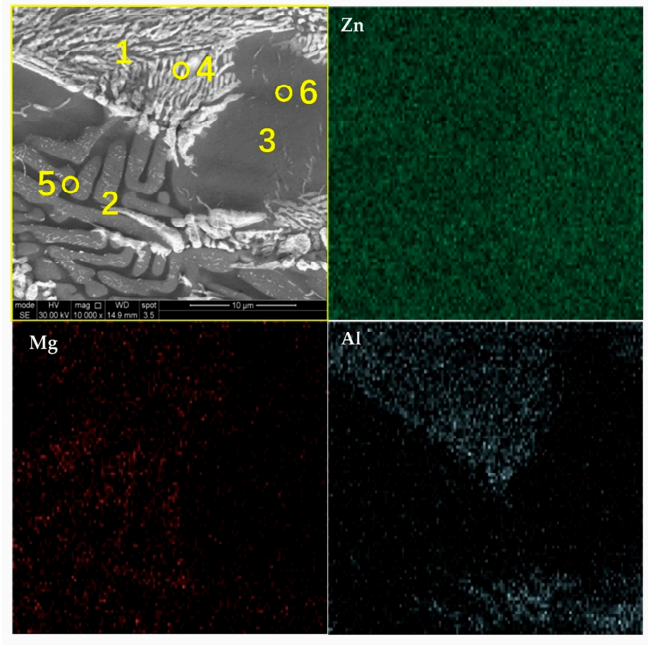
The volume percentages of different phases were analyzed with ImageJ software, converting the SEM images into a binary format and adjusting the threshold to obtain clear-boundary images of different phases. The volume percentage of each phase was obtained using digital statistics algorithms. This study focused on the digital statistical results of both the longitudinal depth and lateral surface, with a 5 mm length and a 5 × 5 mm area for the cross-sectional statistics and the surface statistics, respectively.

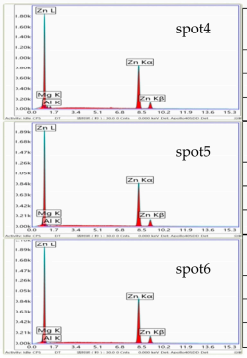
The corrosion resistance of the coatings was tested using a cyclic immersion corrosion test chamber (ZJX-010) at a temperature of 25 °C, and the concentration of the sodium chloride solution was 3.5 wt.%. The other experimental procedures referred to the GB/T 19746-2018 standard [35].

3. Results and Analysis

3.1. Characterization of Coating Phases

The microstructure and phase composition of a coating significantly impact its performance, which directly depends on the types and proportions of the phases. Figure 2 shows the micrographs and EDS (energy spectrum analysis) elemental distribution maps of the Zn-1.6Al-2.0Mg, and it reveals that there were three distinct crystal structures: a spherical monophase structure, a coarse rod-shaped eutectic structure, and a fine rod-shaped eutectic structure. The XRD diffraction patterns of the different coatings are shown in Figure 3, indicating that all coatings contained Zn, Al, and $MgZn_2$ phases. While Zn was the most prominent, $MgZn_2$ and Al phases were present but with lower diffraction peaks.





Element	Weight %	Atoms%	Net strength	Net error
MgK	5	11.88	16.98	0.08
AlK	3.28	7.02	15.05	0.1
Zn	91.73	81.11	503	0.01

Element	Weight %	Atoms%	Net strength	Net error
MgK	2.1	5.4	6.55	0.18
AlK	0.72	1.68	3.14	0.65
Zn	97.18	92.93	518.65	0.01

Element	Weight %	Atoms%	Net strength	Net error
MgK	0.4	1.06	1.27	0.77
AlK	0.54	1.29	2.42	0.67
Zn	99.06	97.65	547.42	0.01

Figure 2. SEM photo of Zn-1.6Al-1.6Mg coating surface, EDS elemental surfaces, and spot scanning results.

The EDS elemental surface distribution scans show that Zn was distributed across the entire surface, Mg was distributed in regions 2 and 3, and Al was distributed only in region 3. According to the solidification curves in Figure 7, Hcp-Zn precipitated at the beginning of solidification, Hcp-Zn and $MgZn_2$ eutectic solidification occurred as the temperature decreased, and finally, Fcc-Al, Hcp-Zn, and $MgZn_2$ eutectic solidification occurred. The atomic fractions in the EDS point analysis indicated that the spot4 position contained both Zn and $MgZn_2$, and the spot5 position contained Zn, $MgZn_2$, and Al.

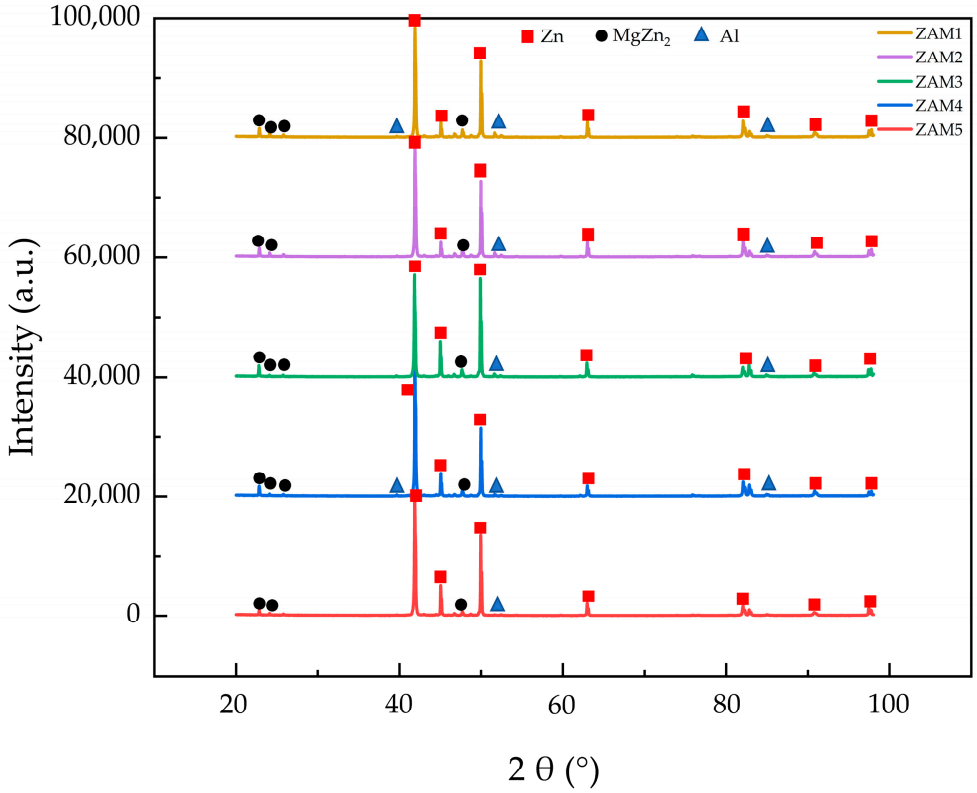


Figure 3. XRD phase analysis of experimental coatings.

This means that the coarse rod-like eutectic structure in region 2 consisted of Zn and $MgZn_2$, and the fine rod-like eutectic structure in region 3 consisted of Zn, $MgZn_2$, and Al. This is consistent with the findings in the literature [1,3]. Bruycker et al. [12] researched the thermodynamics of Zn-3.9Al-2.4Mg coatings and found that the ternary eutectic phases of Hcp-Zn, Fcc-Al, and $MgZn_2$ formed at a certain temperature. They insisted that $MgZn_2$ was formed under rapid cooling conditions instead of thermodynamically stable Mg_2Zn_{11}, which corresponds well to this work [20–23].

Combining the elemental distributions in Figure 2 and the XRD results in Figure 3 (PDF numbers for Zn:96-900-8523; $MgZn_2$:77-1177; and Al:96-901-1603), we identify the spherical monophase structure as Zn, the coarse rod-shaped eutectic structure as a binary eutectic phase of Zn and $MgZn_2$, and the fine rod-shaped eutectic structure as a ternary eutectic phase of Zn, $MgZn_2$, and Al. The Zn element was distributed throughout the coating with a slight decrease at the grain boundaries, while the Mg element presented in the binary and ternary eutectic structures, and the Al element only emerged in the ternary eutectic region. These results are consistent with those previously reported in the literature [12,20].

Under the same process conditions, even a little fluctuation in the composition of the coating will lead to variations in its microstructure and phase composition. With the increase in the Mg/Al ratio, the microstructural types of the different components were similar, which were composed of a zinc-rich phase, a binary eutectic phase, and a ternary eutectic phase, but the proportion of each phase in the different coating compositions was different. The SEM images of the cross-sections and surfaces of the coatings are shown in Figures 4 and 5.

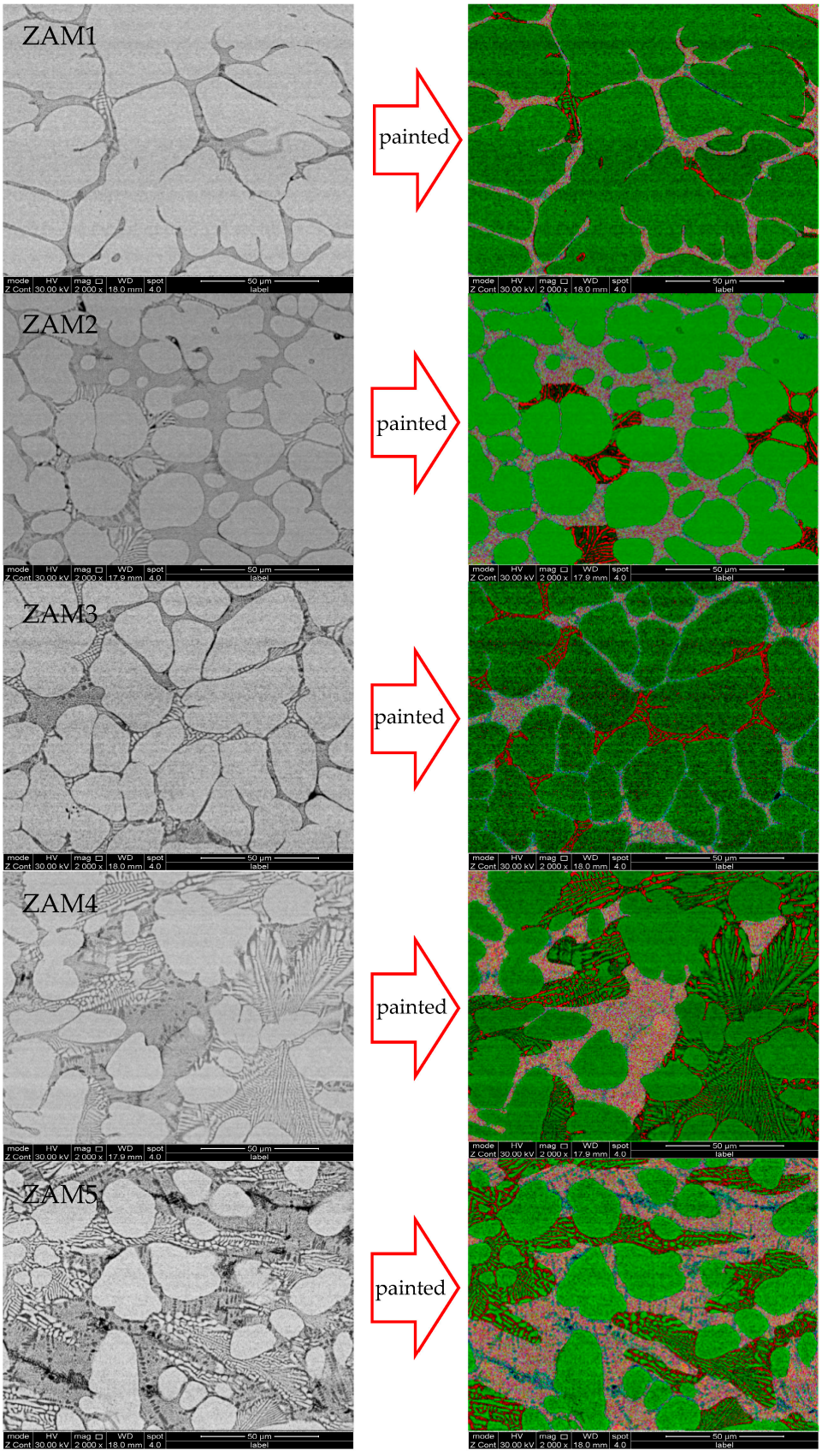


Figure 4. SEM photos of surfaces of coatings and ImageJ dyed alloy phase photos of ZAM1-5.

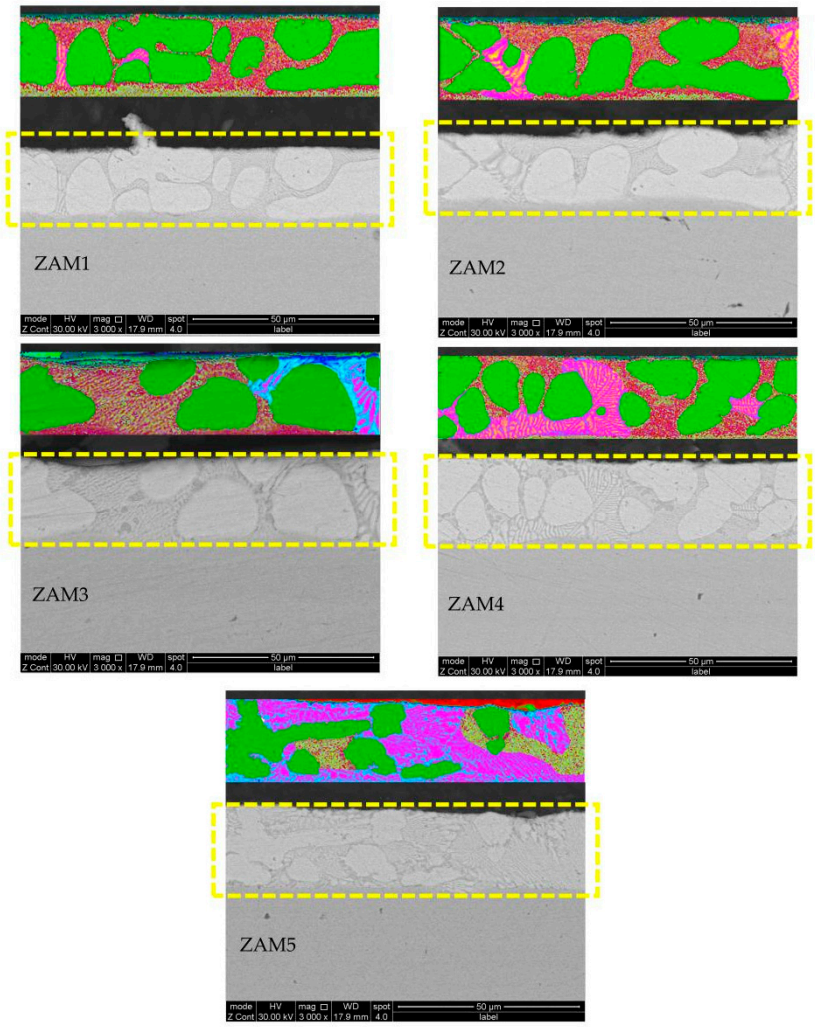


Figure 5. SEM photos of cross-sections of coatings and ImageJ dyed alloy phase photos of ZAM1-5.

In order to quantify the differences in microstructures between the different coatings, ImageJ software was used to stain the surfaces and cross-sectional photographs (Figures 4 and 5), and then the proportions of various phases in the different coatings were statistically analyzed. The statistical results of the proportions of different phases on the surfaces and cross-sections are shown in Figure 6. The results of the surface statistics show that as the magnesium–aluminum ratio increased, the proportions of the binary alloy phases and the ternary alloy phases in the coating gradually increased, while the proportion of zinc-rich phases showed a significant decreasing trend. The results of the cross-sectional statistics show a significant increasing trend in the binary alloy phase, while the ternary alloy phase only presented a slight overall decreasing trend.

The surface and cross-section represent the two dimensions of the plating in the transverse and longitudinal directions, respectively, and the overall phase distribution of the plating can be judged by considering them together. The statistical results of the surfaces and cross-sections of the platings show that the trends of the different phases were consistent, but there were some differences in the ratios of the surface and cross-section phases in the plating with the same Mg-Al ratio. The analysis of the reasons for this variability indicated that this was due to the process conditions of nitrogen purge cooling used in the plating dipping process, which led to different cooling rates in the longitudinal depth of the plating, thus causing the overall microstructure and phase distribution of the plating to differ from the ideal state [1,5,20].

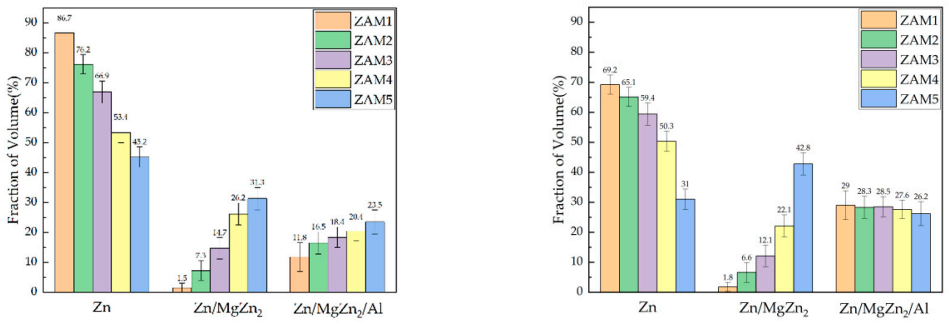


Figure 6. Statistical results of proportions of different dyed phases of ZAM1-5. (**a**) Surfaces of coatings and (**b**) cross-sections of coatings.

The trends of the different phases were consistent in all the examples, corresponding to the statistical results of the coating surfaces and cross-sections, but there was still a difference between the surface and cross-section in the phase ratio of the same magnesium–aluminum coating. The reasons for these differences may be attributed to the nitrogen blow-cooling process, resulting in different cooling rates in the longitudinal depth of the coating, thereby causing differences in the microstructure and phase distribution of the coating compared with the ideal state [1,24].

3.2. Thermodynamic Simulations and Statistical Calculations

Due to the gap between the rapid cooling process and the equilibrium state of the solidified structure, in the equilibrium solidification state, Mg_2Zn_{11} formed, while $MgZn_2$ emerged under non-equilibrium solidification conditions. This may be related to the cooling rate and composition system, whereby both the Mg and Al contents affected the thermodynamic and kinetic conditions of the solidification process [24–28].

Pandat-2023 software was adopted to simulate the solidification process of the five alloy compositions, and the non-equilibrium solidification (Scheil model) curves for the different compositions of the ternary alloy coating are depicted in Figure 7. As the temperature decreased, the liquid phase precipitated a solid Zn-rich phase at first, followed by the appearance of a binary eutectic phase ($Zn/MgZn_2$), and, finally, a ternary eutectic phase ($Zn/MgZn_2/Al$) was generated. With the increase in the Mg/Al ratio, the temperature of the Hcp-Zn at the beginning of solidification gradually decreased, the precipitation temperature of the binary eutectic phase gradually increased, and the temperature of the ternary eutectic phase's precipitation was consistent.

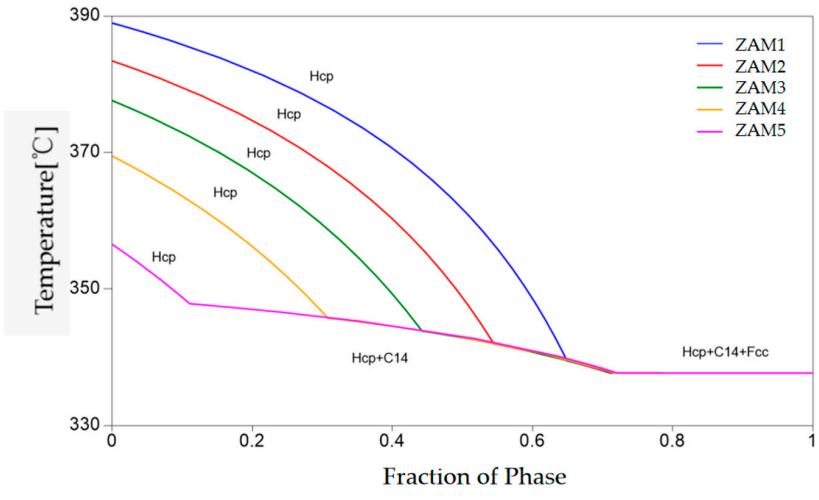
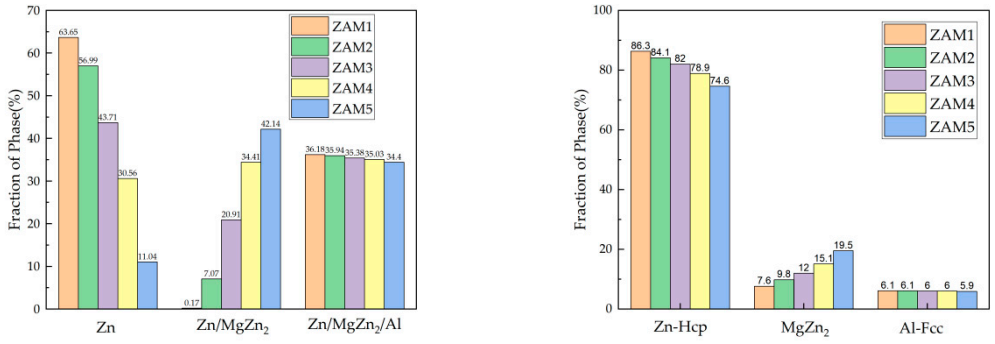


Figure 7. Non-equilibrium solidification (Scheil) curves of different components of ternary alloy coatings.

The non-equilibrium solidification curves of the three components also changed with the variation in the coating composition, as shown in Figure 7. Although the overall solidification reaction was basically the same, there were distinct differences in the conditions of the reaction and the distribution of the final solidified structure. According to the numerical values provided by the software simulation calculation, the proportions of the non-equilibrium solidification phases of the different coatings could be obtained, as shown in Figure 8a. The results show that with the increase in the Mg/Al ratio, the fraction of the binary alloy phase gradually increased, which is consistent with the experimental statistical results. The difference between the ternary eutectic phase and the surface statistical results was due to the uneven cooling rate in the longitudinal depth direction.



(**a**) (**b**)

Figure 8. The results of Pandat simulated non-equilibrium solidification (**a**) phase proportion fractions and (**b**) Zn-Hcp, $MgZn_2$, and Al-Fcc phase proportion fractions.

In addition, it can be seen in Figure 8b that the increase in the Mg/Al ratio directly led to the expansion of the $MgZn_2$ phase. It is worth noting that the Fcc-Al fraction decreased very slightly, while the actual content of Al in all coatings was 1.6 wt.%, which can only exist in the Fcc-Al phase, so the Fcc-Al phase fraction should remain consistent. The reason for this is that the thermodynamic simulation software is based on a theoretical calculation model, which can accurately describe the trends, while it cannot define the precise proportions of actual phase fractions.

3.3. Effect of the Corrosion Performance

In order to investigate the effect of the Al/Mg ratio on the corrosion resistance of the coatings, we compared the corrosion behavior of Zn-Al-Mg coatings with different Mg/Al ratios in a 3.5 wt.% NaCl solution via the macroscopic evaluation of the atmospheric corrosion behavior simulated in a cyclic immersion simulation accelerated experiment. The observed macroscopic corrosion characteristics of the samples after 14 days of testing are shown in Figure 9. Among them, ZAM1 and ZAM2 exhibited red rust as a whole, and the coating protection was basically invalidated; a small amount of speckled red rust appeared on ZAM3-4; and there was no obvious red rust found on ZAM5. Combined with the results of corrosion weight loss in Figure 10, it can be determined that the corrosion performance of the coatings in the NaCl corrosive environment gradually became better with the increase in the Mg/Al ratio.

The Zn-Al-Mg coatings of each composition were subjected to dynamic polarization tests in a 3.5 wt.% NaCl solution, and the corresponding curves are shown in Figure 11. The corrosion potential (E_{corr}) and corrosion current density (I_{corr}) values were calculated using the Tafel method, and the results obtained are shown in Table 2. As the ratio of magnesium to aluminum increased, the corrosion potential (E_{corr}) and corrosion current density (I_{corr}) were lower. This means that the plating with a higher Mg/Al ratio had better sacrificial protection for the steel plate. This was mainly due to the electrochemical reaction of $MgZn_2$ in the coating in the corrosive environment to form a dense protective layer of corrosion

products on the surface of the coating, which improved the protective performance of the coating [27]. The increase in the Mg/Al ratio leading to an increase in the proportion of the $MgZn_2$ alloy phase in the coating was the fundamental reason for the increase in the corrosion resistance.



Figure 9. Macroscopic morphologies of Zn-Al-Mg coatings in cyclic immersion corrosion test after 14 days.

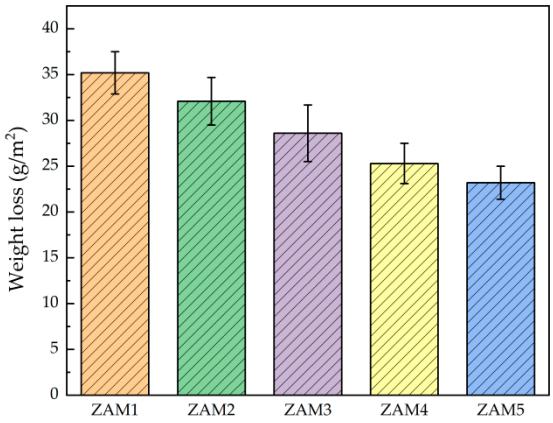


Figure 10. Weight loss of ZAM1-5 coatings after 14 days of immersion corrosion in 3.5 wt.% NaCl solution at 25 °C.

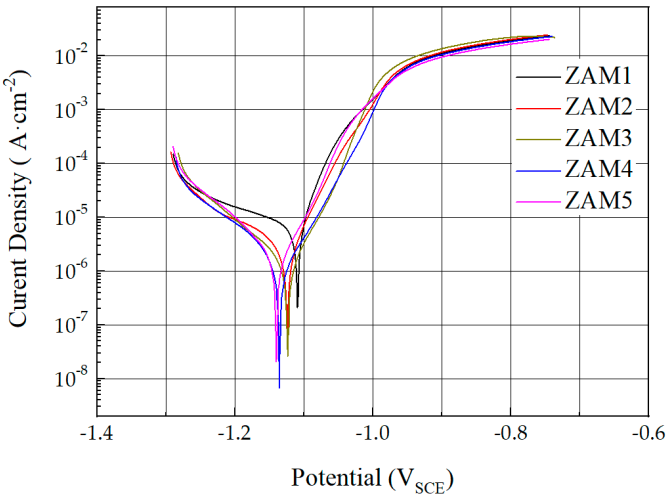


Figure 11. Dynamic polarization curves of experimental coatings in 3.5% NaCl solution.

Table 2. Corrosion potentials and corrosion current densities of experimental coatings.

Coating	E_{corr}, mV_{SCE}	I_{corr}, $\mu A/cm^2$
ZAM1	−1.11	26.6
ZAM2	−1.12	16.7
ZAM3	−1.12	7.40
ZAM4	−1.14	3.86
ZAM5	−1.14	1.29

4. Conclusions

1. The typical microstructure of the Zn-Al-Mg coatings with low aluminum was composed of Hcp-Zn, a binary eutectic phase (Hcp-Zn/$MgZn_2$), and a ternary eutectic phase (Hcp-Zn/$MgZn_2$/Fcc-Al). The content of aluminum was 1.6 wt.%, according to the coloring statistics in the SEM photos of the plated layer. Hcp-Zn decreased with the increase in the Mg/Al ratio, while the binary eutectic phase, in contrast, gradually increased, and the trend of change in the ternary eutectic phase was not obvious.
2. The results of the thermodynamic simulations show that with the increase in the Mg/Al ratio, the $MgZn_2$ phase in the Zn-Al-Mg coatings gradually increased, and the Hcp-Zn phase diminished. Meanwhile, the binary eutectic phase tended to increase, which is consistent with the trend of the statistical results in the coating photos. The tendency of the change in the ternary eutectic phase was not evident, which was mainly due to the same set value of the Al elemental composition in the coating, which means that the change in the ternary eutectic phase mainly depended on the amount of Al added.
3. The cyclic immersion corrosion test showed that the coating with a higher Mg/Al ratio in a 3.5 wt.% NaCl solution possessed better corrosion protection properties, which mainly occurred due to an increase in the proportion of the $MgZn_2$ phase.

The Mg/Al ratio can be used as a reference indicator to evaluate the microstructure of a coating. Under the condition that the production process remains constant, when the Mg/Al ratio changes, the microstructure of the plated coating shows regular evolution, which affects the service performance of the coating. This parameter is very important for the development of new products as a guide, and, at the same time, there are more reference indicators when adding alloy adjustment ingredients to the melt pool.

Author Contributions: Conceptualization, Z.Z. and J.Z.; methodology, Z.Z.; software, Z.Z.; validation, Z.Z., J.Z. and Q.Z.; formal analysis, Z.Z.; investigation, Z.Z.; resources, J.Z. and Q.Z.; data curation, Z.Z. and X.L.; writing—original draft, Z.Z. and X.Z.; writing—review and editing, X.C., S.J. and Q.Z.; visualization, Z.Z. and X.Z.; supervision, J.Z. and Q.Z.; project administration, J.Z.; funding acquisition, Q.Z. All authors have read and agreed to the published version of the manuscript.

Funding: This research received no external funding.

Data Availability Statement: The data presented in this study are available on request from the corresponding author. The data are not publicly available due to the data being used for unpublished PhD thesis.

Conflicts of Interest: Authors Ziyue Zhang, Jie Zhang, Xingyuan Zhao, Xin Liu, Sheming Jiang and Qifu Zhang were employed by the company Central Iron & Steel Research Institute. The remaining authors declare that the research was conducted in the absence of any commercial or financial relationships that could be construed as a potential conflict of interest.

References

1. Yu, K.C.; Li, J.; Liu, X.; Li, J.G.; Xue, X.H. Microstructure of hot-dip galvanized Zn-Al-Mg alloy coating. *J. Shanghai Jiaotong Univ. (Sci.)* **2012**, *17*, 663–667. [CrossRef]
2. Wang, Y.-Q.; Kong, G.; Che, C.-S. Corrosion Behavior of Zn-Al, Zn-Mg, and Zn-Mg-Al Coatings in Simulated Concrete Pore Solution. *Corrosion* **2018**, *75*, 203–209. [CrossRef] [PubMed]

3. Prosek, T.; Hagström, J.; Persson, D.; Fuertes, N.; Lindberg, F.; Chocholatý, O.; Taxén, C.; Šerák, J.; Thierry, D. Effect of the microstructure of Zn-Al and Zn-Al-Mg model alloys on corrosion stability. *Corros. Sci.* **2016**, *110*, 71–81. [CrossRef]
4. Stoulil, J.; Prosek, T.; Nazarov, A.; Oswald, J.; Kriz, P.; Thierry, D. Electrochemical properties of corrosion products formed on Zn-Mg, Zn-Al and Zn-Al-Mg coatings in model atmospheric conditions. *Mater. Corros.* **2015**, *66*, 777–782. [CrossRef]
5. Jiang, S.M.; Yue, C.F.; Zhang, Q.F. Coating Structure and Corrosion Resistance Behavior of Hot Dip Zn-Al-Mg-Si Alloy Coating Steel Sheet. *Adv. Mater. Res.* **2013**, *834–836*, 601–608. [CrossRef]
6. Prosek, T.; Nazarov, A.; Le Gac, A.; Thierry, D. Coil-coated Zn–Mg and Zn–Al–Mg: Effect of climatic parameters on the corrosion at cut edges. *Prog. Org. Coat.* **2015**, *83*, 26–35. [CrossRef]
7. Gogola, P.; Gabalcova, Z.; Kusy, M.; Suchanek, H. The Effect of Sn Addition on Zn-Al-Mg Alloy; Part I: Microstructure and Phase Composition. *Materials* **2021**, *14*, 5404. [CrossRef] [PubMed]
8. Gabalcova, Z.; Gogola, P.; Kusy, M.; Suchanek, H. The Effect of Sn Addition on Zn-Al-Mg Alloy; Part II: Corrosion Behaviour. *Materials* **2021**, *14*, 5290. [CrossRef]
9. Hai Tat, L.; Bakhsheshi-Rad, H.R.; Hamzah, E.; Cho, M.H.; Mostafa, A.; Farahany, S. Microstructure, phase evolution and corrosion behaviour of the Zn–Al–Mg–Sb alloy coating on steel. *Mater. Sci. Technol.* **2019**, *36*, 353–366. [CrossRef]
10. Wang, P.J.; Ma, L.W.; Cheng, X.Q.; Li, X.G. Influence of grain refinement on the corrosion behavior of metallic materials: A review. *Int. J. Miner. Metall. Mater.* **2021**, *28*, 1112–1126. [CrossRef]
11. Li, B.; Dong, A.; Zhu, G.; Chu, S.; Qian, H.; Hu, C.; Sun, B.; Wang, J. Investigation of the corrosion behaviors of continuously hot-dip galvanizing Zn–Mg coating. *Surf. Coat. Technol.* **2012**, *206*, 3989–3999. [CrossRef]
12. De Bruycker, E.; Zermout, Z.; De Cooman, B.C. Zn-Al-Mg Coatings: Thermodynamic Analysis and Microstructure Related Properties. *Mater. Sci. Forum* **2007**, *539–543*, 1276–1281. [CrossRef]
13. Costa, A.N.C.; Silva, G.C.; Ferreira, E.A.; Nakazato, R.Z. Comparative analysis of corrosion resistance of Zinc and Zn-Al-Mg coatings on carbon steel. *Res. Soc. Dev.* **2021**, *10*, e49810111973. [CrossRef]
14. Duchoslav, J.; Arndt, M.; Keppert, T.; Luckeneder, G.; Stifter, D. XPS investigation on the surface chemistry of corrosion products on ZnMgAl-coated steel. *Anal. Bioanal. Chem.* **2013**, *405*, 7133–7144. [CrossRef] [PubMed]
15. Çetinkaya, B.W.; Junge, F.; Müller, G.; Haakmann, F.; Schierbaum, K.; Giza, M. Impact of alkaline and acid treatment on the surface chemistry of a hot-dip galvanized Zn–Al–Mg coating. *J. Mater. Res. Technol.* **2020**, *9*, 16445–16458. [CrossRef]
16. Ahmadi, M.; Salgın, B.; Kooi, B.J.; Pei, Y. Cracking behavior and formability of Zn-Al-Mg coatings: Understanding the influence of steel substrates. *Mater. Des.* **2021**, *212*, 110215. [CrossRef]
17. Lin, S.; Okuda, H.; Matsumoto, K.; Yamaguchi, M.; Sato, K. Nanostructure Distribution and Strengthening Mechanisms in the Interface Regions of Al–Zn/Al–Mg Multilayered Composites. *Mater. Trans.* **2021**, *62*, 603–609. [CrossRef]
18. LeBozec, N.; Thierry, D.; Persson, D.; Riener, C.K.; Luckeneder, G. Influence of microstructure of zinc-aluminium-magnesium alloy coated steel on the corrosion behavior in outdoor marine atmosphere. *Surf. Coat. Technol.* **2019**, *374*, 897–909. [CrossRef]
19. LeBozec, N.; Thierry, D.; Peltola, A.; Luxem, L.; Luckeneder, G.; Marchiaro, G.; Rohwerder, M. Corrosion performance of Zn-Mg-Al coated steel in accelerated corrosion tests used in the automotive industry and field exposures. *Mater. Corros.* **2013**, *64*, 969–978. [CrossRef]
20. Commenda, C.; Pühringer, J. Microstructural characterization and quantification of Zn–Al–Mg surface coatings. *Mater. Charact.* **2010**, *61*, 943–951. [CrossRef]
21. Dutta, M.; Halder, A.K.; Singh, S.B. Morphology and properties of hot dip Zn–Mg and Zn–Mg–Al alloy coatings on steel sheet. *Surf. Coat. Technol.* **2010**, *205*, 2578–2584. [CrossRef]
22. Wint, N.; Cooze, N.; Searle, J.R.; Sullivan, J.H.; Williams, G.; McMurray, H.N.; Luckeneder, G.; Riener, C. The Effect of Microstructural Refinement on the Localized Corrosion of Model Zn-Al-Mg Alloy Coatings on Steel. *J. Electrochem. Soc.* **2019**, *166*, C3147–C3158. [CrossRef]
23. Duchoslav, J.; Arndt, M.; Steinberger, R.; Keppert, T.; Luckeneder, G.; Stellnberger, K.H.; Hagler, J.; Riener, C.K.; Angeli, G.; Stifter, D. Nanoscopic view on the initial stages of corrosion of hot dip galvanized Zn–Mg–Al coatings. *Corros. Sci.* **2014**, *83*, 327–334. [CrossRef]
24. Su, X.; Zhou, J.; Wang, J.; Wu, C.; Liu, Y.; Tu, H.; Peng, H. Thermodynamic analysis and experimental study on the oxidation of the Zn-Al-Mg coating baths. *Appl. Surf. Sci.* **2017**, *396*, 154–160. [CrossRef]
25. Zhang, Z. Microstructure and Corrosion Resistance of Zn-Al-Mg Alloy Diffusion Coating developed on Carbon Steel by Hot Dipping. *Int. J. Electrochem. Sci.* **2020**, *15*, 5512–5519. [CrossRef]
26. Rai, P.K.; Rout, D.; Satish Kumar, D.; Sharma, S.; Balachandran, G. Effect of Magnesium on Corrosion Behavior of Hot-Dip Zn-Al-Mg Coating. *J. Mater. Eng. Perform.* **2021**, *30*, 4138–4147. [CrossRef]
27. Salgueiro Azevedo, M.; Allély, C.; Ogle, K.; Volovitch, P. Corrosion mechanisms of Zn(Mg,Al) coated steel: 2. The effect of Mg and Al alloying on the formation and properties of corrosion products in different electrolytes. *Corros. Sci.* **2015**, *90*, 482–490. [CrossRef]
28. Volovitch, P.; Vu, T.N.; Allély, C.; Abdel Aal, A.; Ogle, K. Understanding corrosion via corrosion product characterization: II. Role of alloying elements in improving the corrosion resistance of Zn–Al–Mg coatings on steel. *Corros. Sci.* **2011**, *53*, 2437–2445. [CrossRef]
29. Thierry, D.; Persson, D.; Luckeneder, G.; Stellnberger, K.-H. Atmospheric corrosion of ZnAlMg coated steel during long term atmospheric weathering at different worldwide exposure sites. *Corros. Sci.* **2019**, *148*, 338–354. [CrossRef]

30. Prosek, T.; Larché, N.; Vlot, M.; Goodwin, F.; Thierry, D. Corrosion performance of Zn-Al-Mg coatings in open and confined zones in conditions simulating automotive applications. *Mater. Corros.* **2010**, *61*, 412–420. [CrossRef]
31. Kim, J.N.; Lee, C.S.; Jin, Y.S. Structure and Stoichiometry of MgxZny in Hot-Dipped Zn–Mg–Al Coating Layer on Interstitial-Free Steel. *Met. Mater. Int.* **2018**, *24*, 1090–1098. [CrossRef]
32. Zhang, Z.; Zhang, J.; Zhao, X.; Cheng, X.; Jiang, S.; Zhang, Q. Effects of Al-Mg on the Microstructure and Phase Distribution of Zn-Al-Mg Coatings. *Metals* **2023**, *13*, 46. [CrossRef]
33. Rai, P.K.; Rout, D.; Kumar, D.S.; Sharma, S.; Balachandran, G. Corrosion behaviour of hot-dip Zn-Al-Mg coatings with different Al content. *Anti-Corros. Methods Mater.* **2022**, *69*, 29–37. [CrossRef]
34. Xu, M.; Han, D.; Zheng, Z.; Ma, R.; Du, A.; Fan, Y.; Zhao, X.; Cao, X. Effects of cooling rate on the microstructure and properties of hot-dipped Zn–Al–Mg coatings. *Surf. Coat. Technol.* **2022**, *444*, 128665. [CrossRef]
35. *GB/T 19746-2018*; Corrosion of Metals and Alloys—Alternate Immersion Test in Salt Solution. Standardization Administration of China: Beijing, China, 2018.

Disclaimer/Publisher's Note: The statements, opinions and data contained in all publications are solely those of the individual author(s) and contributor(s) and not of MDPI and/or the editor(s). MDPI and/or the editor(s) disclaim responsibility for any injury to people or property resulting from any ideas, methods, instructions or products referred to in the content.